Inorganic Chemistry

Article

pubs.acs.org/IC

R_3Au_9Pn (R = Y, Gd−Tm; Pn = Sb, Bi): A Link between $Cu_{10}Sn_3$ and $Gd_{14}Ag_{51}$

Chris Celania,[†,‡] Volodymyr Smetana,[†,‡] Alessia Provino,[†,§,⊥] Vitalij Pecharsky,[†,‡] Pietro Manfrinetti,[†,§,⊥] and Anja-Verena Mudring*[,†,‡,∥]

[†]The Ames Laboratory, U.S. Department of Energy, Iowa State University, Ames, Iowa 50011, United States

[‡]Department of Materials Science and Engineering, Iowa State University, Ames, Iowa 50011, United States

[§]Department of Chemistry, University of Genova, Via Dodecaneso 31, 16146 Genova, Italy

[⊥]Institute SPIN-CNR, Corso Perrone 24, 16152 Genova, Italy

Supporting Information

ABSTRACT: A new series of intermetallic compounds R_3Au_9Pn (R = Y, Gd−Tm; Pn = Sb, Bi) has been discovered during the explorations of the Au-rich parts of rare-earth-containing ternary systems with p-block elements. The existence of the series is strongly restricted by both geometric and electronic factors. R_3Au_9Pn compounds crystallize in the hexagonal crystal system with space group $P6_3/m$ (a = 8.08−8.24 Å, c = 8.98−9.08 Å). All compounds feature Au-Pn, formally anionic, networks built up by layers of alternating edge-sharing Au@Au_6 and Sb@Au_6 trigonal antiprisms of overall composition $Au_{6/2}Pn$ connected through additional Au atoms and separated by a triangular cationic substructure formed by R atoms. From a first look, the series appears to be isostructural with recently reported $R_3Au_7Sn_3$ (a ternary ordered derivative of the $Cu_{10}Sn_3$-structure type), but no example of R_3Au_9M is known when M is a triel or tetrel element. R_3Au_9Pn also contains Au@$Au_6Au_2R_3$ fully capped trigonal prisms, which are found to be isostructural with those found in the well-researched $R_{14}Au_{51}$ series. This structural motif, not present in $R_3Au_7Sn_3$, represents a previously unrecognized link between $Cu_{10}Sn_3$ and $Gd_{14}Ag_{51}$ parent structure types. Magnetic property measurements carried out for Ho_3Au_9Sb reveal a complex magnetic structure characterized by antiferromagnetic interactions at low temperature (T_N = 10 K). Two metamagnetic transitions occur at high field with a change from antiferromagnetic toward ferromagnetic ordering. Density functional theory based computations were performed to understand the materials' properties and to shed some light on the stability ranges. This allowed a better understanding of the bonding pattern, especially of the Au-containing substructure, and elucidation of the role of the third element in the stability of the structure type.

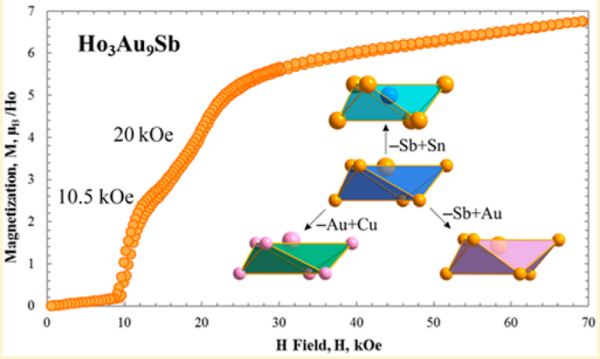

INTRODUCTION

Rare-earth- and gold-containing intermetallic compounds such as those within the R-Au-M family (R = rare earth, M = groups 13−15) have received much research interest in the past few years, with attention recently moving toward the less explored gold-rich regions of the systems.[1−7] Many such compounds show uncommon structural motifs as well as varied electronic and magnetic properties such as ferromagnetism, magnetocaloric effect, superconductivity, and thermoelectricity, among others.

The well-studied relativistic effects on gold's 5d and 6s orbitals often produce notable structural and bonding features, which make it an advantageous component in the search for new intermetallic compounds.[8−14] Examples of gold's versatility in structure and bonding are extensive and include quasicrystals and their approximates,[15−17] as well as unique gold assemblies. Some examples include isolated Au_7 clusters in $A_4Au_7X_2$ (A = K, Rb, Cs; X = Ge, Sn),[18,19] one-dimensional columns such as Au zigzag chains in Ca_3Au_3In,[20] and two-dimensional slabs that are found in K_2Au_3.[21] Three-dimensional gold networks are found in multiple forms such as interconnected trigonal bipyramids found in KAu_5,[22] hexagonal-diamond-like frameworks of Au as seen in the series of Ae-Au-Tr systems,[5,23−28] and combinations of tetrahedral and square-planar Au fragments in Rb_3Au_7.[29]

The shielded 4f electrons of the rare-earth elements deliver the unpaired spins essential to provide a wealth of interesting magnetic properties in their compounds. The varying magnetic moments and atomic sizes moving across the lanthanides allow for fascinating alteration of magnetic interaction. Metals and metalloids from groups 13−15 with radii similar to that of Au (In, Sn, Sb, etc.) may allow significant site mixing and, furthermore, act as a bank of options to tune the valence

Received: April 7, 2017
Published: June 5, 2017

DOI: 10.1021/acs.inorgchem.7b00898
Inorg. Chem. 2017, 56, 7247−7256

Table 1. Crystallographic Details and Refinement Parameters for Y_3Au_9Sb, Gd_3Au_9Sb, Dy_3Au_9Sb, and Gd_3Au_9Bi

	Y_3Au_9Sb	Gd_3Au_9Sb	Dy_3Au_9Sb	Gd_3Au_9Bi
structure type	Gd_3Au_9Sb	Gd_3Au_9Sb	Gd_3Au_9Sb	Gd_3Au_9Sb
formula wt	2381.95	2366.20	2161.18	2453.43
space group	$P6_3/m$ (No. 176)	$P6_3/m$ (No. 176)	$P6_3/m$ (No. 176)	$P6_3/m$ (No. 176)
Z	2	2	2	2
a (Å)	8.127(2)	8.1641(4)	8.127(2)	8.242(2)
c (Å)	9.036(2)	9.0344(6)	8.998(3)	9.055(3)
V (Å^3)	516.9(3)	521.49(6)	514.7(3)	532.7(4)
calcd density (g/cm^3)	13.885	15.069	15.370	15.295
abs coeff μ (mm^{-1})	146.260	147.278	151.670	158.126
$F(000)$	1758	1908	1920	1972
θ range for data collection (deg)	2.894−29.961	2.881−31.886	2.894−28.997	2.854−29.889
index ranges	$-11 \le h, k \le 11, -12 \le l \le 12$	$-11 \le h, k \le 11, -13 \le l \le 13$	$-11 \le h, k \le 11, -12 \le l \le 12$	$-11 \le h, k \le 11, -12 \le l \le 12$
no. of intensity data collected	9542	7512	6642	4449
no. of indep rflns (R_{int})	483 (0.0819)	521 (0.0238)	411 (0.0335)	404 (0.0102)
no. of data/restraints/params	537/0/24	618/0/24	489/0/24	548/0/24
goodness of fit (F^2)	1.132	1.120	1.109	1.035
R1; wR2 ($I_0 > 2\sigma(I)$)	0.0325; 0.0624	0.0238; 0.0446	0.0335; 0.0731	0.0354; 0.0678
R1; wR2 (all data)	0.0399; 0.0644	0.0327; 0.0466	0.0421; 0.0759	0.0604; 0.0749
largest diff peak and hole (e Å−3)	3.889 and −3.558	4.770 and −2.926	3.666 and −3.341	5.192 and −3.856

electron count of the *R*-Au system toward the formation of stable compounds with unprecedented properties.

Within the *R*-Au-*M* family, only a few compounds have been discovered with a concentration of gold of over 50%, making this section particularly interesting for further exploration. Of these compounds, most of the recent research has focused on ternary compounds with tin and has led to the discovery of the $R_3Au_7Sn_3$ series of compounds, which can be described as superstructural polyhedral packing of ZrBeSi type featuring a new homoatomic Au cluster, Au@Au_6.[2,3] However, gold-rich systems in combination with rare-earth elements and group 15 elements are still largely underexplored. The high content of gold allows for a higher chance of homoatomic formations and more opportunities to explore the variety of Au−Au bonding and to investigate the capability of group 15 elements (*Pn*, pnictogens) to stabilize the structures and to affect such formations. The only *R*-Au-*Pn* structure known to date with gold being the majority component is $R(Au_{\sim 0.75}Sb_{\sim 0.25})_2$ (*R* = La, Ce, Pr).[30] These compounds serve as evidence for the ability of group 15 elements such as Sb to induce structural changes and to stabilize new formations. In this work we report on the first example of a gold-rich phase, where the group 15 element acts as an independent constituent and allows for the stabilization of a certain structure type.

EXPERIMENTAL SECTION

Synthesis. Starting materials used for synthesis were Au (99.98%), rare-earth elements (99.9+%) and Bi (99.999%) from the Materials Preparation Center in Ames Laboratory and Sb (99.99%) from Alfa Aesar. Extra Au and Bi were also purchased from MaTeck (99.99%) and Alfa Aesar (99.999%), respectively. A representative of the R_3Au_9Pn series was first observed in the Gd-Au-Sb system as the majority phase in a sample loaded with Gd:Au:Sb in a 2:5:1 ratio that was reacted in a sealed tantalum ampule jacketed in fused silica at 1000 °C for 3 h, followed by annealing at 850 °C for 12 h. Different synthetic conditions were then tested to replicate results, obtain phase-pure R_3Au_9Pn, or test for formation with other rare-earth elements (Y, La−Nd, Sm−Lu tested with Au and Sb) or group 13−15 elements (Al, Ga, In, Sn, Sb, and Bi tested with Gd and Au). The general strategy was to react the starting materials at high temperatures either by heating in an electrical-resistance furnace until at least one component reached liquid state or by arc melting, followed by annealing at lower temperature to create higher quality single crystals for X-ray structure analysis. Samples were typically furnace-cooled as opposed to being quenched back to room temperature. The total mass of samples prepared was 0.5−2.0 g, and all samples were handled under inert conditions (gloveboxes and other similar chambers) using standard techniques (such as oxide removal by surface filing of rare-earth metals).

For the arc-melted samples, ∼6% extra mass of Sb or Bi was added in order to compensate for their loss occurring due to their relatively high vapor pressures. The starting materials (in the form of filings or small chunks) were pressed into a pellet with group 13−15 element pieces placed on one side, which was positioned away from direct contact with the arc. The sample was arc-melted under an inert Ar environment for short periods (∼5 s or until the surface appeared fully molten) and flipped three to four times between each remelting to improve homogeneity. The arc-melted samples were sealed by arc welding into tantalum tubes under an inert Ar atmosphere and then enclosed under vacuum in fused silica tubes and set in a tube furnace for annealing at 850 °C for 2 days, followed by 700 °C for 5 days.

For reactions in resistance furnaces, amounts of *R* elements, Au, and Sb (or Bi) in the stoichiometric ratio 3:9:1 were sealed by arc welding in Ta tubes, closed under vacuum in fused silica casings before high-temperature reaction, and annealing in a tube furnace. The goal of most self-flux reactions is to melt a low-melting component to initiate the reaction with higher melting temperature components such as the rare-earth elements. We note that the temperatures required to initiate reactions are well beyond the melting points for most of the group 13−15 elements tested. Preliminary testing for *R*-Au-Sb (Sb melts at 631 °C) showed that reactions at 850 °C (significantly below the melting point of Au) were not adequate to combine the components. Therefore, the temperature was raised to ensure that the main component, gold, was molten as well. All samples once removed from their various crucibles appeared dark gray with a metallic luster and remained stable in air weeks later.

X-ray Analysis. Samples were examined by X-ray powder diffraction for phase analysis by using either a STOE STADI P diffractometer with a STOE image plate detector or a STOE GmbH Guinier photographic camera with Cu Kα_1; λ = 1.54059 Å (Si as an internal standard, a = 5.4308(1) Å). Powders were prepared by grinding, sieved to 38 μm particles, and either dispersed onto vacuum grease between Mylar sheets and fixed by Al rings or placed on a single-crystal Si zero background plate (depending on the instrument). Data were analyzed using the WinXPow 3.06 and LAZY PULVERIX software packages.[31]

DOI: 10.1021/acs.inorgchem.7b00898
Inorg. Chem. 2017, 56, 7247−7256

Table 2. Atomic Coordinates and Equivalent Isotropic Displacement Parameters for R_3Au_9Pn

atom name	Wyckoff site	x	y	z	U_{eq}
Au1	12*i*	0.36854(7)	0.03302(7)	0.09038(5)	0.0065(2)
Au2	4*f*	1/3	2/3	0.0801(1)	0.0091(2)
Au3	2*c*	2/3	1/3	1/4	0.0083(3)
Y	6*h*	0.2877(2)	0.3219(2)	1/4	0.0043(3)
Sb	2*b*	0	0	0	0.0049(4)
Au1	12*i*	0.37176(5)	0.03425(5)	0.08975(4)	0.0039(1)
Au2	4*f*	1/3	2/3	0.08137(7)	0.0035(1)
Au3	2*c*	2/3	1/3	1/4	0.0054(2)
Gd	6*h*	0.28498(9)	0.32057(8)	1/4	0.0016(1)
Sb	2*b*	0	0	0	0.0010(3)
Au1	12*i*	0.36988(8)	0.03385(8)	0.08978(6)	0.0081(2)
Au2	4*f*	1/3	2/3	0.0826(1)	0.0083(3)
Au3	2*c*	2/3	1/3	1/4	0.0093(3)
Dy	6*h*	0.2864(1)	0.3214(1)	1/4	0.0063(3)
Sb	2*b*	0	0	0	0.0072(5)
Au1	12*i*	0.3754(1)	0.0338(1)	0.09165(8)	0.0108(2)
Au2	4*f*	1/3	2/3	0.0802(1)	0.0110(3)
Au3	2*c*	2/3	1/3	1/4	0.0139(4)
Gd	6*h*	0.2879(2)	0.3238(2)	1/4	0.0087(3)
Bi	2*b*	0	0	0	0.0093(4)

The microstructure and homogeneity of the Tb representative of the series were characterized by optical and scanning electron microscopy (OM and SEM), the latter equipped with an electron microprobe (energy dispersive X-ray analysis, EDS) for semi-quantitative elemental analysis. A Leica Cambridge 360 microscope, equipped with an Oxford X-Max 20 analyzer, was used with Oxford Aztec software, utilizing an extra high-tension voltage of 20.0 kV and probe current of 220 pA. EDS analyses were performed on at least three small areas to identify the phase composition (counting time of 60 s); the accuracy from the EDS is within 1 atom %. The semiquantitative atomic concentration data were also used as a check of results from single-crystal refinement.

Single crystals were selected from crushed sample pieces and affixed to a glass fiber with grease. They were tested at room temperature on either a Bruker APEX CCD diffractometer or a Bruker D8 VENTURE diffractometer (both with Mo Kα radiation; λ = 0.71073 Å), utilizing the APEX 2 and APEX 3 software suites (for the former and latter diffractometers, respectively) for data collection, integration, polarization, and empirical absorption correction.[32,33] Scans typically covered the 2θ range of ~5−63°. The XPREP algorithms in the SHELXTL suite were used to check the intensity data sets for extinction conditions and E statistics necessary, allowing for the assignment of the proper $P6_3/m$ space group. Direct methods were used for the structure solution (SHELXS-97).[34] Structure refinement (refined atomic position, mixed site occupancy, and anisotropic displacement parameters) was carried out with APEX 3 software. For details on the data collection, structure solution, and refinement see Table 1. Table 2 contains the atomic coordinates for Y_3Au_9Sb, Gd_3Au_9Sb, Dy_3Au_9Sb, and Gd_3Au_9Bi. We will discuss the structure of Gd_3Au_9Sb in detail as a representative of the series.

Thermal Analyses. Differential thermal analysis (DTA) was performed on 0.7−0.9 g portions of samples, in either the as-cast or annealed form. Each sample was enclosed in an outgassed Mo crucible by arc welding under an Ar atmosphere and then transferred to the DTA equipment (Netzsch 404 thermal analyzer). Mo crucibles were chosen because of their better refractory properties with respect to Au at the higher temperatures of DTA. Thermal cycles were carried out with rates of 20 °C/min on heating and 10 or 5 °C/min on cooling, under an Ar atmosphere. The accuracy in the temperature measurements was ±5 °C.

Electronic Structure Calculations. Calculations were performed in order to understand the structural preferences, physical properties, and stability ranges of the compounds under investigation. The Vienna ab initio simulation package (VASP)[35−39] was utilized to perform structural optimizations (unit cell volume, shape, and atomic coordinates) prior to any band structure calculations until the energy difference between two iterations fell below 0.01 meV/cell. The DFT (density functional theory) computations in the generalized-gradient approximation (PBE-GGA)[40] were carried out utilizing the projector-augmented wave (PAW) method of Blöchl,[41] as adapted in the VASP code. The energy cutoffs of the plane wave basis sets were set to 500 eV, while starting meshes of up to 8 × 8 × 8 k points were used to sample the first Brillouin zones for reciprocal space integrations.

A chemical bonding map of Y_3Au_9Sb was accomplished on the basis of crystal orbital Hamilton population (COHP) analysis. COHP and its corresponding integrated values (ICOHP) were obtained in two ways—using the tight-binding linear-muffin-tin orbital (TB-LMTO) method with the atomic sphere approximation (ASA) in the Stuttgart code.[42,43] For the TB-LMTO-ASA calculations Wigner−Seitz spheres (WS) and empty spheres (ES) were automatically assigned, in order to best approximate the overlapping potentials in line with the full potentials. The following orbitals were utilized in the basis set (downfolded[44] orbitals in parentheses): Au 6*s*/6*p*/5*d*/(5*f*); Y 5*s*/(5*p*)/4*d*/(4*f*); Sb 5*s*/5*p*/(5*d*)/(4*f*). The corresponding WS radii were as follows (Å): Au, 1.60, 1.60 and 1.62; Y, 1.85; Sb: 1.82. Reciprocal space integrations were performed with the tetrahedron method[45] using 312 irreducible k points.

Physical Property Measurements. dc magnetization data for the Ho_3Au_9Sb single-phase sample was collected in a Quantum Design MPMS (magnetic property measurement system) SQUID (superconducting quantum interference device) magnetometer. A powder specimen of ~20 mg was placed in a fused silica sample holder that was made gastight using Teflon tape. The sample was first tested in a DC field of 1 kOe over a temperature range of 2−300 K in order to determine the magnetic behavior and possible critical temperature locations. Isothermal magnetization measurement at 2 K followed with fields up to ±70 kOe. Finally, further DC measurements in fields of 5, 15, and 40 kOe were performed (temperature ranges of 2−250, 2−300, and 2−300 K, respectively).

RESULTS AND DISCUSSION

Crystal Chemistry. Crystals of sufficient quality for single-crystal X-ray diffraction analysis could be obtained for Y_3Au_9Sb, Gd_3Au_9Sb, Dy_3Au_9Sb, and Gd_3Au_9Bi. Structure analysis for Gd_3Au_9Sb reveals a complex 3D gold network comprised of Au@Au_{6+2} bicapped trigonal prisms and Sb@Au_6 trigonal

DOI: 10.1021/acs.inorgchem.7b00898
Inorg. Chem. 2017, 56, 7247−7256

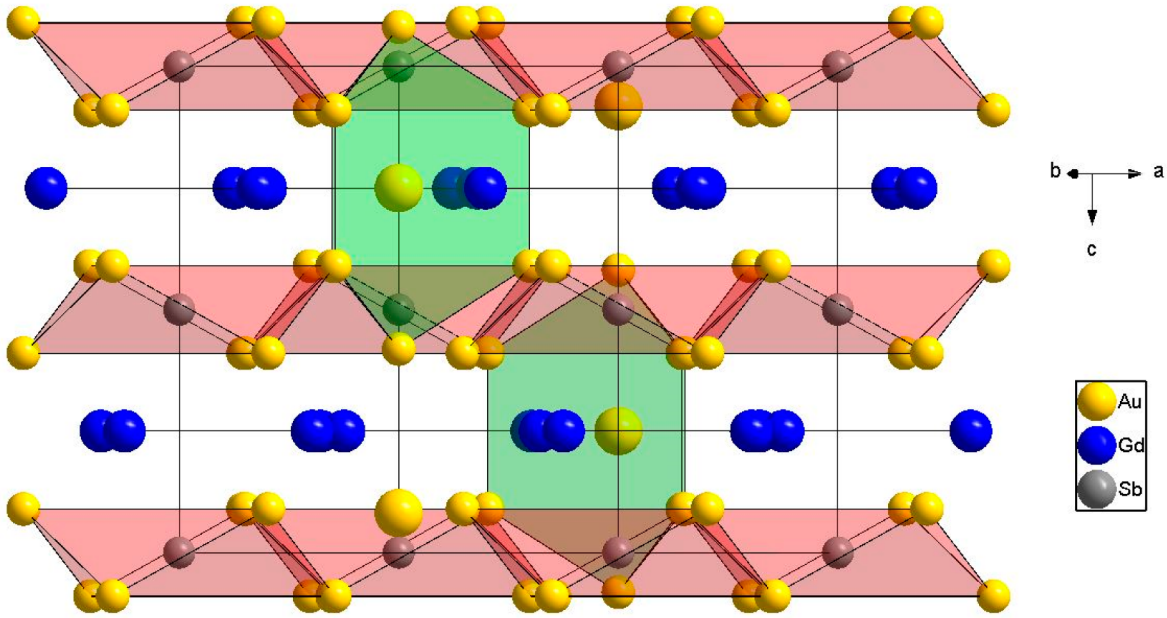

Figure 1. Representation of the crystal structure of Gd_3Au_9Sb. The three main fragments characterizing the structure are noticeable. The green bicapped trigonal prisms denote $Au@Au_8$ units. The red polyhedra denote $Sb@Au_6$ trigonal antiprisms that share vertices with the basal planes of the bicapped trigonal prisms. Trigonal planes of Gd are in plane with the center atom of the bicapped trigonal prisms, as shown in the following figures.

Table 3. Lattice Parameters (a and c), Observed Unit Cell Volume (V_{obs}), and Formation Volume ($\Delta V\%$) for R_3Au_9Pn (Pn = Sb, Bi)

	lattice parameters				
R_3Au_9Sb	a (Å)	c (Å)	V_{obs} (Å^3)	$\Delta V\%$ from Gd_3Au_9Sb PXRD	obtained by
Gd_3Au_9Sb	8.1641(4)	9.0344(6)	521.49(1)		SCXRD
Gd_3Au_9Sb	8.1809(1)	9.0751(1)	526.00(9)	0	PXRD
Tb_3Au_9Sb	8.1432(3)	9.0345(7)	518.83(9)	−7.17	PXRD
Dy_3Au_9Sb	8.127(2)	8.998(3)	514.6(8)	−11.3	SCXRD
Ho_3Au_9Sb	8.1083(3)	9.0059(7)	512.76(4)	−13.25	PXRD
Er_3Au_9Sb	8.0800(1)	8.9773(3)	507.57(4)	−18.44	PXRD
Tm_3Au_9Sb	8.079(1)	8.977(1)	507.4(3)	−18.61	PXRD
Y_3Au_9Sb	8.1327(6)	9.0486(1)	518.30(1)	−7.71	PXRD
Y_3Au_9Sb	8.1274(2)	9.036(2)	516.9(3)		SCXRD
Gd_3Au_9Bi	8.242(2)	9.055(3)	532.7(4)	+12.7	SCXRD

antiprisms as the most characteristic features (Figure 1). Layers of alternating edge-sharing $Au@Au_6$ and $Sb@Au_6$ trigonal antiprisms are connected through the layers of interchanging Au atoms (which are the capping atoms of the $Au@Au_6$ trigonal antiprisms) and R triangles. The interatomic Au−Au distances within the central $Au@Au_6$ cluster range between 2.8242(4) and 2.8955(7) Å, being consistent with the sum of corresponding covalent radii, and are similar to those found in other Au-rich intermetallics.[2,3] It is worth noting that the Au−Au contacts between the central position and the surrounding trigonal prism in $Au@Au_6$ are the shortest gold contacts in the structure, while the distances to the Au atoms capping the trigonal prism are fairly long (2.9937(6) Å). The distances between the capping gold atoms of the $Au@Au_{6+2}$ prism and the Au vertices of other, nearby $Sb@Au_6$ antiprisms (2.8758(5) Å) are also appropriate distances for Au−Au interactions. Thus, a rather extended network of gold atoms is formed. The only known formations similar to the $Au@Au_{6+2}$ prisms appear to be $Au@Au_8$ clusters that are stabilized with phosphine and form different conformations.[46] A noncentered, "naked" Au_9 cluster has also been predicted by density functional theory (DFT) to be stable in the gas phase.[47]

Gadolinium atoms cap all three rectangular faces of the $Au@Au_{6+2}$ polyhedra with a distance of 3.0654(6) Å from the central gold atom and 3.1175(6) Å to the gold atoms on the rectangular faces. In summary, a fully capped trigonal prism $Au@Au_6Au_2Gd_3$ is formed around the central gold atom. The $Au@Au_6Au_2Gd_3$ units similarly form layers through Au vertex sharing with $Sb@Au_6$ antiprisms. The Sb−Au distances are fairly long at 3.0165(4) Å (in comparison to the sum of their theoretical covalent radii, 2.850 Å[50]). However, the Au−Au distances along the edges of the Au antiprism around the central Sb atom are, within values of 3.3274(5) and 5.0323(2) Å, even longer in comparison to the sum of the covalent radii for gold, 2.880 Å. The second coordination sphere of Sb includes two Gd triangles (3.3578(5) Å), resulting in an overall coordination number of 12 and an icosahedron as the coordination polyhedron. The gadolinium atoms themselves form a slightly distorted triangular network (due to inclusion of Au atoms), with three different interatomic distances

DOI: 10.1021/acs.inorgchem.7b00898
Inorg. Chem. 2017, 56, 7247−7256

(4.3036(2), 4.5904(2), and 5.3094(3) Å); see Figure S2 in the Supporting Information. The longest distance refers to the Gd−Gd distances of a triangle surrounding the Au3 position, while the two shorter distances refer to Gd−Gd distances of two other triangles not centered by atoms. However, all three distances are noticeably longer than the covalent radii sum of 3.580 Å.[50]

Unit cell parameters of the other isotypic R_3Au_9Pn compounds were derived from X-ray powder diffraction data. Their values are in line with the expectations from the lanthanide contraction, as well as with the increase in atomic size from Sb to Bi (Table 3). The average covalent radius[48] of R atoms used in forming R_3Au_9Pn is 1.92 Å, somewhat below the average of 1.96 Å forming the structurally similar $R_3Au_7Sn_3$ phase, while the radii of Au, Sn, and Sb are all nearly identical (1.36, 1.39, and 1.39 Å, respectively). However, R_3Au_9Pn only formed for covalent radii ratios of R/Au between 1.40 and 1.44 but allowed for more variation with R/Pn: from Y/Sb (1.28) to Gd/Bi (1.41).

The R_3Au_9Pn structure is closely related to the structure reported for the $R_3Au_7Sn_3$ series,[2,3] where both can be viewed as ordered representatives of the $Cu_{10}Sn_3$ structure type.[49] If one rewrites the formula of $R_3Au_7Sn_3$ as $R_3Au_7Sn'_2Sn''$, the compositional relationships become more evident; replacing Sn′ by Au and Sn″ by Sb leads to R_3Au_9Sb. The Au substitution also leads to some decrease in the unit cell volume (∼4%) followed by a rather large increase (∼22%) in density. However, upon substitution of Sn by Au, the atomic position of the latter shifts slightly farther away from the center plane of the slab. Figure 2 displays a comparison of the common

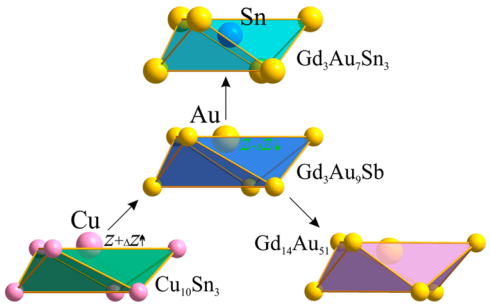

Figure 2. Variation of the common building unit in the crystal structures of $Cu_{10}Sn_3$, $R_3Au_7Sn_3$, R_3Au_9Pn, and $Gd_{14}Au_{51}$.

building unit in the crystal structures of $Cu_{10}Sn_3$, $R_3Au_7Sn_3$, R_3Au_9Pn, and $Gd_{14}Au_{51}$. From this viewpoint, the Gd_3Au_9Sb type appears to be a missing link connecting the two known binary types $Cu_{10}Sn_3$ and $Gd_{14}Ag_{51}$ and the recently discovered $Gd_3Au_7Sn_3$. On the other hand, R_3Au_9Pn is compositionally situated between $R_3Au_7Sn_3$ and $R_{14}Au_{51}$ or, more importantly, its ternary representatives $R_{14}(Au,M)_{51}$ (M = group 13−15).[50,51] The latter is known with all rare earths and several transition metals and may accommodate the majority of post-transition metals. The crystal structure of $R_{14}(Au,M)_{51}$, due to a slightly different R content, contains similar Au-centered and noncentered fully capped trigonal prisms complemented by interpenetrated Frank−Kasper polyhedra centered on the R sites along the z axis. A representation outlining similar polyhedra between $Gd_{14}Au_{51}$ and Gd_3Au_9Sb structures is found in Figure S3 in the Supporting Information. Indeed, it was found that the $R_{14}(Au,M)_{51}$ phase is a strong competitor of R_3Au_9Pn, melting congruently at much higher temperatures, and being just a few atom % away compositionally (having visible homogeneity ranges). In fact, 12 of 15 unique elemental combinations used in attempts to synthesize R_3Au_9Pn yielded $R_{14}(Au,M)_{51}$, and 9 of those cases formed $R_{14}(Au,M)_{51}$ as the majority component, as evidenced by PXRD.

Scanning electron microscopy analysis for a sample of nominal Tb_3Au_9Sb, revealed two similar but distinct phases: the phases appear discrete within the micrographs (Figure 3), and

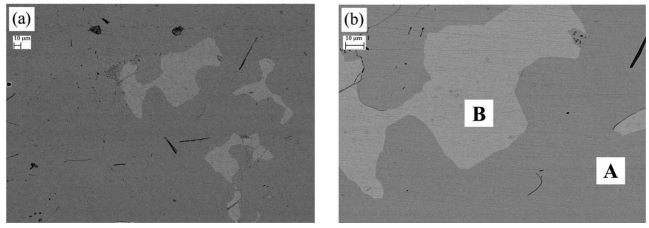

Figure 3. (a) SEM micrograph (backscattering mode) of a sample with nominal composition Tb_3Au_9Sb. (b) Portion of sample, at higher magnification, used for EDS analysis. Data corresponding to the phases A (Tb_3Au_9Sb) and B ($Tb_{14}(Au,Sb)_{51}$) can be found in Table 3.

the dark and light phases correspond to Tb_3Au_9Sb and $Tb_{14}(Au,Sb)_{51}$, respectively. The EDS data are collected and summarized in Table 4. These values support the proposed

Table 4. EDS Data Corresponding to the SEM Images of a Tb DTA Sample with Nominal Composition Tb_3Au_9Sb (See Figure 3)[a]

	average (overall)		dark phase (A)		light phase (B) (≤3 vol %)	
element	wt %	atom %	wt %	atom %	wt %	atom %
Tb	18.93	21.78	19.23	22.08	17.67	20.75
Au	75.87	70.41	75.39	69.86	80.24	76.04
Sb	5.2	7.8	5.38	8.06	2.09	3.21

[a]The phase with higher terbium content shows a composition similar to the expected atomic percentages for the Tb_3Au_9Sb phase, while that with the lower terbium content suggests the $Tb_{14}(Au,Sb)_{51}$ phase.

formula for the Tb_3Au_9Sb compound and indicate the existence of the compositionally similar ternary $Tb_{14}(Au,Sb)_{51}$ solid solution phase (as well the amount of Au−Sb mixing within). It is expected that the R_3Au_9Pn phases (Pn = Sb, Bi) do not form (or have very restricted and as yet unobserved existence ranges) for all rare earths. For example, no lanthanides lighter than Gd formed R_3Au_9Sb, often preferring the $R_{14}(Au,M)_{51}$ structure, allowing the R_3Au_9Pn phases to play a role as a structural connection between $R_3Au_7Sn_3$ and $R_{14}(Au,M)_{51}$. In this view, $R_3Au_7Sn_3$ appears as a byproduct, which is stabilized by insertion of a heteroatom in the center of the other systems' $Au@Au_6$ trigonal prisms.

Physical Properties. To elucidate on the magnetic properties, the magnetization for phase-pure Ho_3Au_9Sb (PXRD pattern shown in Figure S4 in the Supporting Information) was measured as a function of temperature, $M(T)$, in applied magnetic fields of 1 kOe (between 2 and 250 K). A sharp peak at around 10 K in the magnetization curve can be associated with a paramagnetic (PM) to antiferromagnetic (AFM) transition (inset of Figure 4). The isothermal magnetization, $M(H)$, was measured at T = 2 K (below the critical temperature) and between ±70 kOe (Figure 5). The data show a peculiar behavior for this compound: from 0 to

DOI: 10.1021/acs.inorgchem.7b00898
Inorg. Chem. 2017, 56, 7247−7256

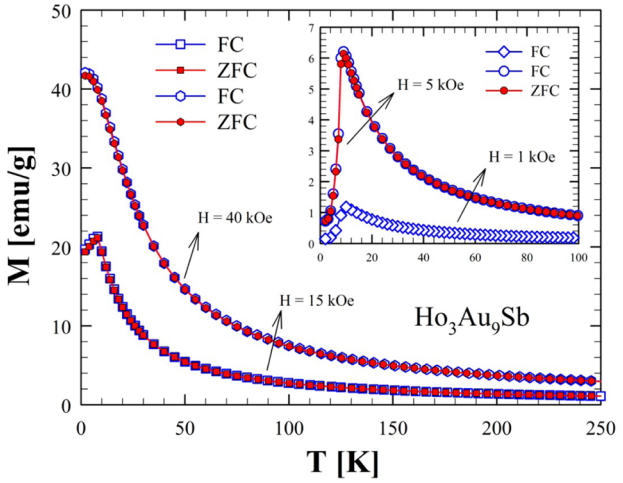

Figure 4. Magnetization versus temperature for Ho_3Au_9Sb measured in applied magnetic fields of 1 and 5 kOe (top right inset) and 15 and 40 kOe between 2 and 250 K.

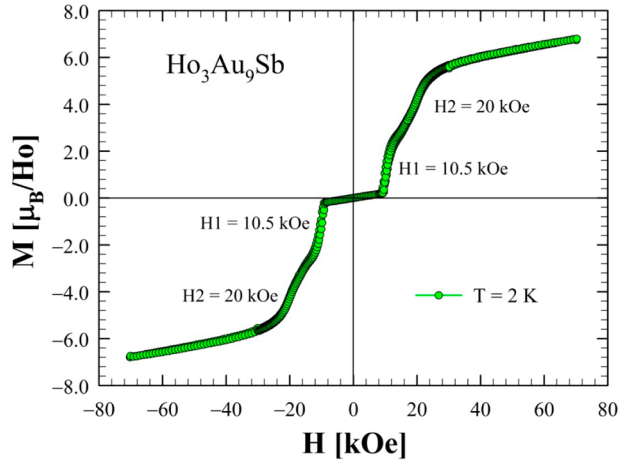

Figure 5. Isothermal magnetization measured at T = 2 K between −70 and 70 kOe for Ho_3Au_9Sb. Transition field values are given alongside the curves.

about 10 kOe the behavior is typical of an AFM material, with the magnetization weakly and almost linearly increasing with increasing magnetic field. Then, two field-induced metamagnetic transitions take place at 10.5 kOe (H_1) and 20 kOe (H_2), as determined from the maxima of the first derivative of the magnetization versus the applied magnetic field, dM/dH (Figure S5 in the Supporting Information). A small, though noticeable, hysteresis is also present after the first transition (Figure S5). Even at the highest applied field of 70 kOe, the magnetization keeps increasing without reaching gJ = 10 μ_B/Ho^{3+}. This implies that either the ferromagnetic state is not collinear or crystalline electric field effects are quite substantial. Neutron diffraction investigation as a function of magnetic field would be necessary to shed light on the complex magnetic behavior of this compound.

The two transitions noted in the isothermal magnetization data prompted further field-cooled (FC) and zero-field-cooled (ZFC) $M(T)$ measurements at fields congruent with the three regions separated by the transitions: 5 kOe (before H_1), 15 kOe (before H_2), and 40 kOe (after H_2). The first was measured between 2 and 250 K, while the latter two were between 2 and 300 K (Figure 4). The data in both the 1 and 5 kOe curves show a trend typical of an AFM behavior where the magnetization approaches nearly zero value below T_N. Meanwhile, the data at 15 and 40 kOe better represent the behavior of a FM-like material due to the much higher magnetizations below T_N.

The inverse magnetic susceptibility, $1/\chi$, plotted against temperature was used to determine the Weiss temperature (Θ_P) and the effective moment (μ_{eff}) using the Curie–Weiss law, $\chi = C/(T - \Theta_P)$, as illustrated in Figure 6. The Weiss

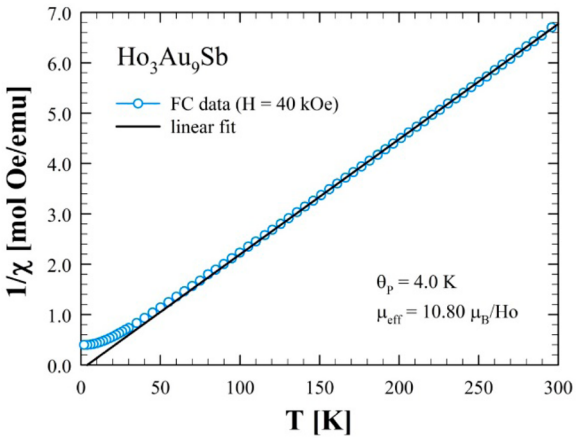

Figure 6. Curie–Weiss fitting of field-cooled inverse susceptibility curve over the 2–300 K temperature range for a 40 kOe field.

temperature is slightly positive (4.0 K), pointing to a ferromagnetic ground state. The effective moment per rare-earth atom (10.80 μ_B/Ho^{3+}) is close to the expected theoretical value calculated from Hund's rule for noninteracting Ho^{3+} ions (10.60 μ_B/Ho^{3+}).[52]

Analogous to the $R_3Au_7Sn_3$ structure, the triangular R lattice in R_3Au_9Pn does not indicate geometrical spin frustration. For $R_3Au_7Sn_3$, the low-temperature, low-field ordering predicted on the basis of total energy calculations is spin-up across a layer and spin-down in the opposite layer as described for $Gd_3Au_7Sn_3$.[2] Possible ferrimagnetic (FIM) ordering in R_3Au_9Pn appears unlikely, due to a single R site and its triangular lattice. Reported low-field measurements for $R_3Au_7Sn_3$ compounds all similarly show low-temperature transitions from a PM state to AFM.[2,3] $Nd_3Au_7Sn_3$ and $Tb_3Au_7Sn_3$ also appear to undergo metamagnetic field induced transitions from an AFM state to FIM/FM. However, these transitions are less sharp than either of the transitions observed in Ho_3Au_9Sb. Transitions from PM to AFM were also noted for $R_{14}Ag_{51}$ compounds (for R = Gd, Tb)[53,54] which, despite the comparable centered and noncentered fully capped trigonal prisms, do not share the triangular, planar rare-earth structure because of the additional R positions at the centers of the interpenetrated Frank–Kasper polyhedra.

Electronic Structures. The existence of two structurally related but compositionally different $R_3Au_7Tt_3$ and R_3Au_9Pn series of compounds with tetrels and pnictogens points toward a strong influence of electronic factors, while formal electron-counting rules do not provide any help. In spite of the significantly lower number of valence electrons in the latter, the compounds exist, yet with fewer of the rare-earth elements as a side effect of geometric factors. On the other hand, all attempts to substitute Pn with triel or tetrels failed. The electronic

DOI: 10.1021/acs.inorgchem.7b00898
Inorg. Chem. 2017, 56, 7247–7256

structure of Y_3Au_9Sb was investigated as a prototype for the series to obtain a better understanding of this phenomenon and to predict further possibilities for the extended family.

The electronic density of states (DOS) curves for Y_3Au_9Sb reveal broad valence bands reaching −10 eV and large Au 5*d* contributions between 2.5 and 6.5 eV below the Fermi level (E_F) (Figure 7a). The Au bands are dominant through the

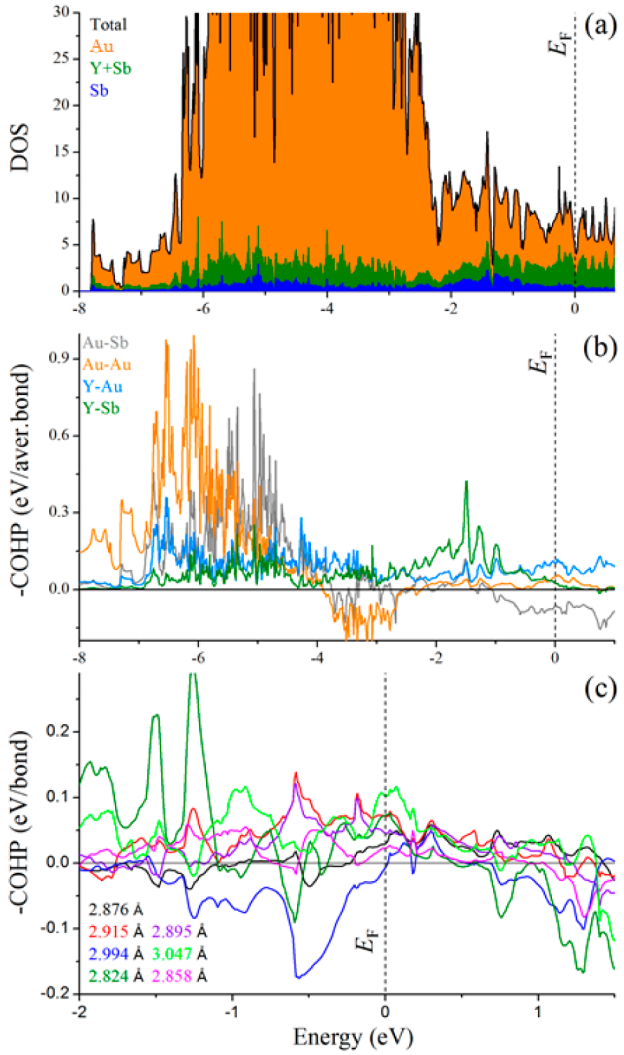

Figure 7. Plots of (a) total and projected DOS curves for Y_3Au_9Sb and (b) average and (c) interaction projected COHP curves. The Fermi level is represented by dashed lines.

entire region, while Y contributions become significant starting from −1 eV and above and Sb contributions remain relatively small above −8 eV (in accordance with its concentration in the compound). This picture is rather typical for a number of related Au-rich phases in the *A*-Au-*E* systems (*A* = active metal, *E* = post transition element).[2,3,25,55] A more interesting situation is observed around the Fermi level. The DOS regions exhibit nonzero values, pointing toward metallic characteristics, as can also be confirmed by the band structure plot (Figure S6 in the Supporting Information). Despite the presence of many local minima, there is a clear relatively deep but narrow pseudogap at E_F. This feature of its electronic structure is in good agreement not only with the strong restriction for post transition elements but also with the absence of any detectable

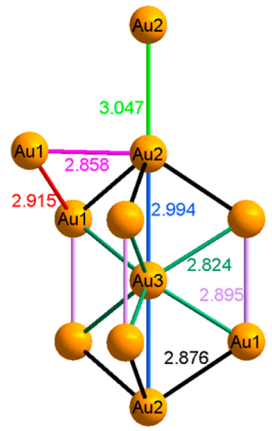

Figure 8. Interatomic Au−Au contacts in Å around Au_9 formation as observed in the crystal structure of Y_3Au_9Sb.

mixing in any site of the crystal structure. This LMTO model of the electronic structure confirms the absence of R_3Au_9Tt compounds and suggests the existence of the R_3Au_9Tr compounds, which have not yet been detected. On the other hand, the chemistry of indides and antimonides is very different, in part due to the $5s^2$ lone pair in the latter, leading to the formation of homoatomic fragments and networks.[56] Such an electron configuration differs from triels and tetrels, i.e. indium or tin, and affects Au−Sb and *R*−Sb bonding, as will be discussed below.

A closer inspection of the previously reported electronic structure of the $R_3Au_7Sn_3$ series[2,3] showed a well detectable local minimum at ∼7 e/fu less with respect to the investigated composition and rather huge pseudogap starting at the Fermi level. Our initial attempts to obtain such a compound by replacing all Au positions in the structure by Pt (1 e/a less) failed, apparently due to the much higher location of the Pt 5d band and switch of the potential pseudogap into the regions of extremely high density of states. The "solution" was unexpectedly found through the decrease of the post transition element proportion along with the exchange of the latter. Finally, the electronic densities of states for the binary $Cu_{10}Sn_3$ exhibit a local minimum at E_F and a distinct pseudogap at 3 e/fu, more indication of further possibilities of Cu exchange with more electron-rich components.

The mystery remains that the existence of each subgroup is restricted to a specific post transition metal. As we mentioned above, the crystal structures of R_3Au_9Pn and $R_3Au_7Tt_3$ do not belong to the same structure type but are rather very close relatives. On the other hand, we know $Au_{10}In_3$[57] to be an example of a strong distortion of the $Cu_{10}Sn_3$ type. What factors are the most important for formation and stabilization of all these modifications? Every structure comes up with its own valence electron concentration (vec) values, which are not so close to each other even within the same group. While the $Au_{10}In_3$ representatives[58,59] are restricted to 19 e/fu, the $Cu_{10}Sn_3$ type spans a wide range from 21 to 28 e/fu. Geometric factors and electronegativities have also been considered as possible factors influencing the type preference, but no clear difference has been detected. Moreover, partial overlap of the main criteria occurs for all considered cases. Let us consider changes within three different subgroups on the basis of the transition element proportion in $Cu_{10}Sn_3$, $Y_3Au_7Sn_3$, and Y_3Au_9Sb. The most affected unit in all of the structures is the not entirely isolated $M^I_6M^{II}$ cluster (M^I = Au, Cu, M^{II} = Sn, Sb,

DOI: 10.1021/acs.inorgchem.7b00898
Inorg. Chem. 2017, 56, 7247−7256

Au). The position of the central atom is moving from nearly the center of the unit closer to the face and finally out of the Au_6 trigonal antiprism (Figure 8). Such an atomic rearrangement, in spite of the same quantity and type of Wyckoff positions, does not allow us to consider all three examples as representatives of a single structure type in terms of bonding. This fact may also explain a lower importance of the vec factor for the group in general; however, it does not neglect its role in each separate case.

To learn more about the structural stability and variability and the role of local changes in these processes, we continued with COHP analysis of the interatomic interactions. The COHP curves for the selected contacts are shown in Figure 7b,c, while the corresponding ICOHP values are summarized in Table 5. The first unexpected result appeared from the bonding

Table 5. Bond Lengths and ICOHP Values for the Selected Interactions in Y_3Au_9Sb

bond type	length (Å)	−ICOHP/bond (eV)	no./ cell	−ICOHP (eV)	contribn (%)
Au−Au	2.824	1.26	12	15.12	14.04
Au−Au	2.858	1.25	12	15	13.93
Au−Au	2.876	1.08	6	6.48	6.02
Au−Au	2.895	1.27	6	7.62	7.08
Au−Au	2.916	1.08	6	6.48	6.02
Au−Au	2.994	0.78	4	3.12	2.90
Au−Au	3.046	1.10	2	2.2	2.04
Au−Sb	3.017	1.06	12	12.72	11.81
Y−Au	3.044	0.73	26	18.98	17.63
Y−Au	3.117	0.65	20	13	12.08
Y−Sb	3.358	0.64	12	6.4	7.13
Y−Y	4.303	0.07	6	0.42	0.39
Y−Y	4.591	0.02	6	0.12	0.11

pattern of Au−Sb pairs, showing strong antibonding interactions at the Fermi level and nearby. The position of the E_F at the local minimum of the antibonding region suggests some island of stability, but in general a much higher number of electrons would be required to move this interaction into the bonding region. A very different picture has been observed for $Y_3Au_7Sn_3$, where all Au−Sn and Au−Au interactions were found to be bonding or optimized up to the Fermi level, and a larger number of electrons is not anticipated. Such a picture is indeed in good agreement with the observed Au−Sb bond lengths and may partially explain the lower proportion of Sb in the compound in comparison to Sn in the $R_3Au_7Sn_3$ phases. The limited number of Au−Sb bonds does not play the major role in the general picture; however, an increase in Sb concentration would lead to a higher number of antibonding interactions and structural instability.

The most interesting question in Y_3Au_9Sb is the significance of orbital interactions within the extended Au network, particularly in the formal Au_9 unit. Analysis of the various Au−Au pairs (Figure 7c) revealed characteristic differences for both intra- and intercluster separations depending on direction. The most populated Au−Au bonds occur in the center of the Au_9 unit (a bicapped-trigonal-prismatic Au_7 cluster) and between its vertices and Au(2) positions, axially capping the neighboring Au_7 trigonal prism. Six Au(2) atoms, with the shortest distances to the central Au_7 unit, are common for three such units, leading to the formulation $Au@Au_6Au_{6/3} = Au@Au_8 = Au_9$. Despite the identical look, this formulation proves the concept of a layered structure normal to the c axis. It is also worth noting that Au(3)−Au(2) interactions are strongly antibonding below the Fermi level, are rather nonbonding at E_F, and show the lowest −ICOHP values in comparison to all others and even longer Au(2)−Au(2) intercluster contacts.

Highly populated homoatomic Au−Au contacts together with relatively long and less populated Au−M contacts (M = post transition element) does not constitute the usual picture for the majority of the investigated A−Au−Tr systems.[55,60,61] This bonding picture may serve as an extra proof why no R_3Au_9M compound has been observed with In, Ga, or Al. Another interesting fact is the rather high contributions from the heteroatomic Y−Au and Y−Sb contacts, showing greater involvement of rare-earth elements in the covalent interactions. Such a picture is very atypical for the light active metals; however, relatively high contributions have been detected for some phases with Na and Ba.[15,62] It is not unexpected that Au−Au contacts provide the greatest contribution to the total orbital interactions (Table 5), but the −ICOHP values of 0.6−0.7 eV/bond for the Y-containing pairs guarantee the second place for the formal cation-containing pairs, being comparable to or even exceeding the contribution from the Au−Sb pairs.

SUMMARY

The new series of isostructural Au-rich intermetallic compounds with general formula R_3Au_9Pn has been discovered and investigated, being restricted to the majority of the heavy lanthanides or Y and heavy pnictides. The compounds crystallize in a hexagonal unit cell with its own structure type (Gd_3Au_9Sb type), which is closely related to $Cu_{10}Sn_3$ and $Gd_3Au_7Sn_3$ and provides an excellent possibility for analyzing the influence of all possible factors on the phase formation and stability of $Cu_{10}Sn_3$-related compounds. $Au@Au_6Au_2R_3$ fully capped trigonal prisms found within the R_3Au_9Pn series, isostructural with those of the $R_{14}Au_{51}$ series, create a structural link between the parent structures ($Cu_{10}Sn_3$ and $Gd_{14}Ag_{51}$), complementing the compositional similarities between the R_3Au_9Pn and $R_{14}Au_{51}$ series. Structural analysis and electronic structure calculations revealed $Au_9 = Au@Au_6Au_{6/3}$ as the main building block of the anionic network, in contrast to the more intuitive $Au@Au_6Au_2$ bicapped trigonal prism. The shift of the Au position with respect to the center of trigonal-antiprismatic slabs from one type to another, which occurs because of changing strength and type of interatomic interactions, explains the failure of electron-counting rules, the lower importance of electronegativities, and geometric criteria in the hypothetically common structure type stability. Magnetization measurements in Ho_3Au_9Sb revealed antiferromagnetic ordering, with a Néel temperature of 10 K; metamagnetic transitions observed with increasing magnetic field at 2 K suggest that a ferromagnetic state can be stabilized at high fields. Overall, the comparison with several closely related structure types allows for an explanation of structural changes, tuning of physical properties, and simplification of the search for new representatives in unexplored systems.

ASSOCIATED CONTENT

Supporting Information

The Supporting Information is available free of charge on the ACS Publications website at DOI: 10.1021/acs.inorgchem.7b00898.

DOI: 10.1021/acs.inorgchem.7b00898
Inorg. Chem. 2017, 56, 7247−7256

Thermal treatments of various samples, atomic displacement parameters for Gd_3Au_9Sb, alternate representation of the layered structure (Au/Sb slabs and Gd/Au triangular plane), comparison of R_3Au_9Pn and $R_{14}Au_{51}$ polyhedra, hysteresis and critical field data for Ho_3Au_9Sb, band structure of Y_3Au_9Sb, PXRD pattern and Rietveld refinement for Ho_3Au_9Sb, and DSC data from the relevant segment for Ho_3Au_9Sb (PDF)

Accession Codes

CCDC 1551596−1551599 contain the supplementary crystallographic data for this paper. These data can be obtained free of charge via www.ccdc.cam.ac.uk/data_request/cif, or by emailing data_request@ccdc.cam.ac.uk, or by contacting The Cambridge Crystallographic Data Centre, 12 Union Road, Cambridge CB2 1EZ, UK; fax: +44 1223 336033.

AUTHOR INFORMATION

Corresponding Author

*E-mail for A.-V.M.: anja-verena.mudring@mmk.su.se; anja.mudring@rub.de.

ORCID

Volodymyr Smetana: 0000-0003-0763-1457

Alessia Provino: 0000-0002-7577-6642

Anja-Verena Mudring: 0000-0002-2800-1684

Present Address

[‖]Department of Materials and Environmental Chemistry, Stockholm University, Svante Arrhenius väg 16C, 10691 Stockholm, Sweden; email: anja-verena.mudring@mmk.su.se.

Notes

The authors declare no competing financial interest.

ACKNOWLEDGMENTS

The Ames Laboratory is operated for the U.S. Department of Energy by Iowa State University of Science and Technology under Contract No. DE-AC02-07CH11358. This work was supported by the Department of Energy, Office of Basic Energy Sciences, Materials Sciences Division.

REFERENCES

(1) Fickenscher, T.; Rodewald, U.; Pottgen, R. Ternary stannides $RE_2Au_5Sn_2$ (RE = Gd-Er)-i3 superstructures of the Fe_2P type. *Z. Kristallogr. - Cryst. Mater.* **2015**, *230*, 117−122.

(2) Provino, A.; Steinberg, S.; Smetana, V.; Kulkarni, R.; Dhar, S.; Manfrinetti, P.; Mudring, A. Gold-rich $R_3Au_7Sn_3$: establishing the interdependence between electronic features and physical properties. *J. Mater. Chem. C* **2015**, *3*, 8311−8321.

(3) Provino, A.; Steinberg, S.; Smetana, V.; Paramanik, U.; Manfrinetti, P.; Dhar, S. K.; Mudring, A.-V. Gold in the layered structures of $R_3Au_7Sn_3$: from relativity to versatility. *Cryst. Growth Des.* **2016**, *16*, 5657−5668.

(4) Gebresenbut, G.; Tamura, R.; Eklöf, D.; Gomez, C. Syntheses optimization, structural and thermoelectric properties of 1/1 Tsai-type quasicrystal approximants in RE-Au-SM systems (RE = Yb, Gd and SM = Si, Ge). *J. Phys.: Condens. Matter* **2013**, *25*, 135402.

(5) Smetana, V.; Steinberg, S.; Card, N.; Mudring, A.; Miller, G. Crystal Structure and Bonding in $BaAu_5Ga_2$ and $AeAu_{4+x}Ga_{3-x}$ (Ae = Ba and Eu): Hexagonal Diamond-Type Au Frameworks and Remarkable Cation/Anion Partitioning in the Ae-Au-Ga Systems. *Inorg. Chem.* **2015**, *54*, 1010−1018.

(6) Bigun, I.; Steinberg, S.; Smetana, V.; Mudryk, Y.; Kalychak, Y.; Havela, L.; Pecharsky, V.; Mudring, A.-V. Magnetocaloric behavior in ternary europium indides EuT5In: probing the design capability of first-principles-based methods on the multifaceted magnetic materials. *Chem. Mater.* **2017**, *29*, 2599−2614.

(7) Smetana, V.; Steinberg, S.; Mudryk, Y.; Pecharsky, V.; Miller, G. J.; Mudring, A.-V. Cation-poor complex metallic alloys in Ba(Eu)−Au−Al(Ga) systems: identifying the keys that control structural arrangements and atom distributions at the atomic level. *Inorg. Chem.* **2015**, *54*, 10296−10308.

(8) Pitzer, K. S. Relativistic effects on chemical properties. *Acc. Chem. Res.* **1979**, *12*, 271−276.

(9) Pyykkö, P.; Desclaux, J. P. Relativity and the periodic system of elements. *Acc. Chem. Res.* **1979**, *12*, 276−281.

(10) Pyykkö, P. Relativistic Effects in Structural Chemistry. *Chem. Rev.* **1988**, *88*, 563−594.

(11) Pyykkö, P.; Johnson, M.; Martinez, T. Relativistic effects in chemistry: more common than you thought. *Annu. Rev. Phys. Chem.* **2012**, *63*, 45−64.

(12) Schwerdtfeger, P.; Bast, R.; Gerry, M.; Jacob, C.; Jansen, M.; Kello, V.; Mudring, A.; Sadlej, A.; Saue, T.; Sohnel, T.; Wagner, F. The quadrupole moment of the 3/2(+) nuclear ground state of Au-197 from electric field gradient relativistic coupled cluster and density-functional theory of small molecules and the solid state. *J. Chem. Phys.* **2005**, *122*, 124317.

(13) Mudring, A.; Jansen, M.; Daniels, J.; Kramer, S.; Mehring, M.; Ramalho, J.; Romero, A.; Parrinello, M. Cesiumauride ammonia (1/1), CsAu center dot NH_3: A crystalline analogue to alkali metals dissolved in ammonia? *Angew. Chem., Int. Ed.* **2002**, *41*, 120−124.

(14) Mudring, A.; Jansen, M. Base-induced disproportionation of elemental gold. *Angew. Chem., Int. Ed.* **2000**, *39*, 3066−3067.

(15) Smetana, V.; Lin, Q.; Pratt, D. K.; Kreyssig, A.; Ramazanoglu, M.; Corbett, J. D.; Goldman, A. I.; Miller, G. J. A sodium-containing quasicrystal: using gold to enhance sodium's covalency in intermetallic compounds. *Angew. Chem., Int. Ed.* **2012**, *51*, 12699−12702.

(16) Lin, Q.; Corbett, J. Development of the Ca-Au-In icosahedral quasicrystal and two crystalline approximants: Practice via pseudogap electronic tuning. *J. Am. Chem. Soc.* **2007**, *129*, 6789−6797.

(17) Lin, Q.; Corbett, J. Approximant phases and an icosahedral quasicrystal in the Ca-Au-Ga system: The influence of size of gallium versus indium. *Inorg. Chem.* **2008**, *47*, 7651−7659.

(18) Sinnen, H.-D.; Schuster, H.-U. $Rb_4Au_7Sn_2$, eine intermetallische Phase mit siebenatomigen Goldclustern/ $Rb_4Au_7Sn_2$, an Intermetallic Phase with Sevenatomic Gold-Clusters. *Z. Naturforsch., B: J. Chem. Sci.* **1981**, *36*, 833.

(19) Zachwieja, U.; Wlodarski, J. $Cs_4Au_7Sn_2$: a gold tin framework structure with Au_7 clusters and Sn_2 dumb-bells. *Z. Anorg. Allg. Chem.* **1998**, *624*, 1443−1446.

(20) Muts, I.; Zaremba, V.; Rodewald, U.; Pottgen, R. Infinite gold zig-zag chains as structural motif in Ca_3Au_3In - A ternary ordered variant of the Ni_4B_3 type. *Z. Anorg. Allg. Chem.* **2008**, *634*, 56−60.

(21) Kriegerbeck, P.; Brodbeck, A.; Strahle, J. Synthesis and structure of K_2Au_3, a new phase in the system potassium gold. *Z. Naturforsch. B* **1989**, *44*, 237−239.

(22) Zachwieja, U. Single-crystal growth and strucrural refinement of KAu_5 and $RbAu_5$. *J. Alloys Compd.* **1993**, *196*, 187−190.

(23) Palasyuk, A.; Grin, Y.; Miller, G. J. Turning gold into "diamond": a family of hexagonal diamond-type Au-frameworks interconnected by triangular clusters in the Sr−Al−Au system. *J. Am. Chem. Soc.* **2014**, *136*, 3108−3117.

(24) Seidel, S.; Hoffmann, R.-D.; Pöttgen, R. $SrAu_4Ga_3$: a further example with Ga_3 units and a Lonsdaleite-related gold substructure. *Monatsh. Chem.* **2014**, *145*, 1043−1049.

(25) Lin, Q.; Mishra, T.; Corbett, J. D. *J. Am. Chem. Soc.* **2013**, *135*, 11023−11031.

(26) Gerke, B.; Hoffmann, R.-D.; Pöttgen, R. Zn_3 and Ga_3 triangles as building units in $Sr_2Au_6Zn_3$ and $Sr_2Au_6Ga_3$. *Z. Anorg. Allg. Chem.* **2013**, *639*, 2444−2449.

(27) Gerke, B.; Pottgen, R. $Sr_2Au_6Al_3$ and $Eu_2Au_6Al_3$ - First Representatives of the $Sr_2Au_6Zn_3$ Type with Aluminum Triangles. *Z. Naturforsch. B* **2014**, *69*, 121−124.

DOI: 10.1021/acs.inorgchem.7b00898
Inorg. Chem. 2017, 56, 7247−7256

(28) Gerke, B.; Korthaus, A.; Niehaus, O.; Haarmann, F.; Pöttgen, R. Triangular Zn_3 and Ga_3 units in $Sr_2Au_6Zn_3$, $Eu_2Au_6Zn_3$, $Sr_2Au_6Ga_3$, and $Eu_2Au_6Ga_3$ − structure, magnetism, 151Eu Mössbauer and $^{69;71}$Ga solid state NMR spectroscopy. *Z. Naturforsch. B* **2016**, *71*, 567−577.
(29) Zachwieja, U. A new compound in the rubidium gold system - synthesis and structure of Rb_3Au_7. *J. Alloys Compd.* **1993**, *199*, 115−118.
(30) Salamakha, L. P.; Sologub, O. L.; Gonçalves, A. P.; Mudryi, S. I.; Almeida, M. $R(Au_{0.75}Sb_{0.25})_2$ (R = La, Ce, Pr) with UHg_2 structure type, new members of the AlB_2 family. *J. Alloys Compd.* **2007**, *429*, 140−142.
(31) *WinXPow 3.06 and LAZY PULVERIX*; Stoe & Cie, Darmstadt, Germany, 2004.
(32) Blessing, R. H. An empirical correction for absorption anisotropy. *Acta Crystallogr., Sect. A: Found. Crystallogr.* **1995**, *51*, 33−38.
(33) *APEX 2 and APEX 3*; Bruker AXS, Madison, WI, 1996.
(34) Sheldrick, G. M. A short history of SHELX. *Acta Crystallogr., Sect. A: Found. Crystallogr.* **2008**, *64*, 112−122.
(35) Kresse, G.; Marsman, M.; Furthmüller, J. *Vienna Ab Initio Simulation Package (VASP)*; The Guide Universität Wien, Vienna, Austria, 2010.
(36) Kresse, G.; Furthmüller, J. Efficiency of ab-initio total energy calculations for metals and semiconductors using a plane-wave basis set. *Comput. Mater. Sci.* **1996**, *6*, 15−50.
(37) Kresse, G.; Furthmüller, J. Efficient iterative schemes for ab initio total-energy calculations using a plane-wave basis set. *Phys. Rev. B: Condens. Matter Mater. Phys.* **1996**, *54*, 11169−11186.
(38) Kresse, G.; Hafner, J. Ab initio molecular dynamics for liquid metals. *Phys. Rev. B: Condens. Matter Mater. Phys.* **1993**, *47*, 558−561.
(39) Kresse, G.; Joubert, D. From ultrasoft pseudopotentials to the projector augmented-wave method. *Phys. Rev. B: Condens. Matter Mater. Phys.* **1999**, *59*, 1758−1775.
(40) Perdew, J. P.; Burke, K.; Ernzenhof, M. Generalized gradient approximation made simple. *Phys. Rev. Lett.* **1996**, *77*, 3865−3868.
(41) Blöchl, P. E. Projector augmented-wave method. *Phys. Rev. B: Condens. Matter Mater. Phys.* **1994**, *50*, 17953−17979.
(42) Tank, R.; Jepsen, O.; Burkhardt, A.; Andersen, O. K. Max-Planck-Institut für Festkörperforschung, Stuttgart, Germany, 1994.
(43) Andersen, O. K.; Jepsen, O. Explicit, first-principles tight-binding theory. *Phys. Rev. Lett.* **1984**, *53*, 2571−2574.
(44) Lambrecht, W. R. L.; Andersen, O. K. Donwfold tech. *Phys. Rev. B: Condens. Matter Mater. Phys.* **1986**, *34*, 2439−2449.
(45) Blöchl, P. E.; Jepsen, O.; Andersen, O. K. Tetrahedron method. *Phys. Rev. B: Condens. Matter Mater. Phys.* **1994**, *49*, 16223−16233.
(46) Qiu, Y.; Wang, S. Theoretical Investigations of Phosphine-stabilization on Gold Cluster $[Au@Au_8(PR3)_8]^{3+}$ (R = Me, OMe, H, F, Cl, CN). *Chem. J. Chinese U.* **2012**, *33*, 2549−2555.
(47) Wells, D.; Delgass, W.; Thomson, K. Density functional theory investigation of gold cluster geometry and gas-phase reactivity with O-2. *J. Chem. Phys.* **2002**, *117*, 10597−10603.
(48) Cordero, B.; Gomez, V.; Platero-Prats, A. E.; Reves, M.; Echeverria, J.; Cremades, E.; Barragan, F.; Alvarez, S. Covalent radii revisited. *Dalton Trans.* **2008**, 2832−2838.
(49) Lenz, J.; Schubert, K. Crystal structure of $Cu_{10}Sn_3$ (m). *Monatsh. Chem.* **1971**, *102*, 1689−1698.
(50) Lin, Q.; Corbett, J. D. $Ca_{14}Au_{46}Sn_5$: a "colored" $Gd_{14}Ag_{51}$-type structure containing columns of well-differentiated hexagonal gold stars. *Inorg. Chem.* **2011**, *50*, 1808−1815.
(51) Verbovytsky, Y. New ternary phases from the *R*-Au-Ga systems (*R* = Gd-Tm). *Chem. Met. Alloys* **2014**, *7*, 42−55.
(52) Cotton, S. *Lanthanide and Actinide Chemistry*; Wiley: Chichester, U.K., 2006.
(53) Fischer, P.; Pomjakushin, V.; Keller, L.; Daoud-Aladine, A.; Sikora, W.; Dommann, A.; Hulliger, F. Antiferromagnetic three-sublattice Tb ordering in $Tb_{14}Ag_{51}$. *Phys. Rev. B: Condens. Matter Mater. Phys.* **2005**, *72*, 134413.
(54) Tambornino, F.; Sappl, J.; Hoch, C. The $Gd_{14}Ag_{51}$ structure type and its relation to some complex amalgam structures. *J. Alloys Compd.* **2015**, *618*, 326−335.
(55) Smetana, V.; Miller, G. J.; Corbett, J. D. Polyclusters and Substitution Effects in the Na−Au−Ga System: Remarkable Sodium Bonding Characteristics in Polar Intermetallics. *Inorg. Chem.* **2013**, *52*, 12502−12510.
(56) A. Papoian, G.; Hoffmann, R. Hypervalent Bonding in One, Two, and Three Dimensions: Extending the Zintl−Klemm Concept to Nonclassical Electron-Rich Networks. *Angew. Chem., Int. Ed.* **2000**, *39*, 2408−2448.
(57) Jandali, M. Z.; Rajasekharan, T.; Shchubert, K. Crystal structure of $Au_{10}In_3$. *Z. Metallkd.* **1982**, *73*, 463−467.
(58) Schubert, K.; Balk, M.; Bhan, S.; Breimer, H.; Esslinger, P.; Stolz, E. Einige strukturelle Ergebnisse an metallischen Phasen IV. *Naturwissenschaften* **1959**, *46*, 647−648.
(59) Guenzel, E.; Schubert, K. Strukturuntersuchungen im System Kupfer-Antimon. *Z. Metallkd.* **1958**, *49*, 433−439.
(60) Smetana, V.; Corbett, J. D.; Miller, G. J. Four polyanionic compounds in the K−Au−Ga system: a case study in exploratory synthesis and of the art of structural analysis. *Inorg. Chem.* **2012**, *51*, 1695−1702.
(61) Smetana, V.; Miller, G. J.; Corbett, J. D. Three alkali-metal-gold-gallium systems. Ternary tunnel structures and some problems with poorly ordered cations. *Inorg. Chem.* **2012**, *51*, 7711−7721.
(62) Zhang, H.; Borrmann, H.; Oeschler, N.; Candolfi, C.; Schnelle, W.; Schmidt, M.; Burkhardt, U.; Baitinger, M.; Zhao, J.-T.; Grin, Y. Atomic Interactions in the p-Type Clathrate I $Ba_8Au_{5.3}Ge_{40.7}$. *Inorg. Chem.* **2011**, *50*, 1250−1257.

DOI: 10.1021/acs.inorgchem.7b00898
Inorg. Chem. 2017, 56, 7247−7256